Enhancing CO₂ Electroreduction to Ethanol on Copper-Silver Composites by Opening an Alternative Catalytic Pathway

Louisa Rui Lin Ting,[1,2,†] Oriol Piqué,[3,†] Si Ying Lim,[1,2] Mohammad Tanhaei,[4] Federico Calle-Vallejo,[3,*] and Boon Siang Yeo[1,2,*]

[1] Department of Chemistry, National University of Singapore, 3 Science Drive 3, Singapore 117543.

[2] Solar Energy Research Institute of Singapore, National University of Singapore, 7 Engineering Drive 1, Singapore 117574.

[3] Departament de Ciència de Materials i Química Física & Institut de Química Teòrica i Computacional (IQTCUB), Universitat de Barcelona, Martí i Franquès 1, 08028 Barcelona, Spain.

[4] Institute of Materials Research and Engineering, Agency for Science, Technology and Research, 2 Fusionopolis Way, Singapore 138634.

* To whom correspondence should be addressed to: chmyeos@nus.edu.sg, f.calle.vallejo@ub.edu

† These authors contributed equally to this work.

1 **Abstract**

2 A fundamental question in the electrochemical CO_2 reduction reaction (CO_2RR) is how to

3 rationally control the catalytic selectivity. For instance, adding a CO-producing metal like Ag

4 to Cu shifts the latter's CO_2RR selectivity towards C_2 products, but the underlying cause of the

5 change is unclear. Herein, we show that CuAg boundaries facilitate the coupling of carbon-

6 containing species to give ethanol, through an otherwise closed pathway. Oxide-derived Cu

7 nanowires mixed with 20 nm Ag particles (Cu:Ag mole ratio of 1:20) reduce CO_2 to ethanol

8 with a current density of -4.1 mA/cm^2 at -1.1 V vs. RHE and ethanol/ethylene Faradaic

9 efficiency ratio of 1.1. These figures of merit are respectively 5 and 3 times higher than those

10 for pure oxide-derived Cu nanowires. CO_2RR using different Ag:Cu ratios and Ag particle

11 sizes reveals that ethanol production scales with CO production on the Ag sites and the

12 abundance of CuAg boundaries, and, very interestingly, without significant modifications to

13 ethylene formation. Computational modelling shows selective ethanol evolution via Langmuir-

14 Hinshelwood $*CO + *CH_x$ (x = 1, 2) coupling at CuAg boundaries, and that the formation of

15 energy-intensive CO dimers is circumvented.

16

17 **Keywords**

18 Electrochemical CO_2 reduction, electrocatalysis, ethanol, copper-silver, reaction mechanism

1 Introduction

The electrochemical reduction of carbon dioxide (CO_2RR), when driven by renewable electricity, provides a carbon-neutral route to generate fuels and chemical feedstock.[1] Metallic copper foils can catalyse the electroreduction of CO_2 to hydrocarbons, such as methane and ethylene, and oxygenates such as ethanol.[2] Regrettably, they are not particularly selective towards C_2 molecules.[3] Oxidizing the Cu electrodes prior to their use as catalysts enhances C_2 product selectivity, with ethylene more prevalently formed over ethanol.[4-6] This raises the question of how to strategically steer the conversion of CO_2 towards ethanol, which is both a widely-used commodity chemical and a fuel with one of the highest gravimetric energy densities.[7] Techno-economic analyses also highlight the importance of good ethanol selectivity in order to increase the technology readiness level (TRL) of CO_2-to-ethanol electrolysers.[7-8] In this context, elucidating the reaction intermediates and pathways of CO_2RR to ethanol is a key requisite.

For the production of C_2 molecules on Cu surfaces, *CO dimerisation has been identified as the key step in the reaction pathway.[9-10] Theoretical simulations on Cu(100) further suggested that in the late stages of the pathway, there is a selectivity-determining intermediate, namely *CH_2CHO.[11] The hydrogenation of this intermediate leads to either ethylene or acetaldehyde,[11] which is readily electroreduced to ethanol.[9, 12-13] The idea of a shared ethanol/ethylene pathway is supported by the Faradaic efficiencies (FE) of the two products being modified similarly in presence of alkaline cations.[14]

An alternative pathway for the reduction of CO_2 to ethanol involving the coupling of CO and CH_x intermediates to give acetaldehyde, which again reduces to ethanol, has also been proposed.[15] This pathway has been postulated to occur when there is an excess of CO on the working catalyst.[16] Previously, zinc, a selective CO-producing metal, was added as a co-catalyst to copper. The Zn sites would produce CO molecules *in-situ*, which would combine

44   with *CH$_x$ moieties on the Cu sites to produce C$_2$ species.[16] By increasing the amount of Zn in

45   the bimetallic catalysts, it was found that the selectivity of ethanol versus ethylene production,

46   defined by the ratio of their Faradaic efficiencies (FE$_{ethanol}$/FE$_{ethylene}$), could increase by a factor

47   of up to ~12.5. Ethanol formation was maximized on Cu$_4$Zn at −1.05 V vs. RHE, with a

48   Faradaic efficiency and current density of 29.1% and -8.2 mA/cm^2, respectively. Lee et al

49   further studied oxide-derived CuAg catalysts and reported a maximum FE$_{ethanol}$ of 34.8%

50   at -1.2 V vs RHE.[17] At the same potential, ethylene was produced with a FE of 9.5%.

51   Maximising the number of biphasic CuAg boundaries was hypothesized to facilitate migration

52   of CO produced on Ag sites to the Cu sites where ethanol could be eventually formed.

53   Recently, various copper-silver catalysts have been reported to exhibit enhanced

54   CO$_2$RR selectivity and activity towards multi-carbon products. The enhancement has been

55   attributed to the suppression of the competing hydrogen evolution reaction,[18-19] optimised

56   binding of reaction intermediates such as *CO,[20-21] and increased surface population of *CO

57   intermediates on the catalysts.[22-24] Propositions to improve multi-carbon product selectivity

58   include optimising copper-silver interfaces to boost CO migration from silver to copper sites,[17,

59   [23-24] and mixing copper and silver phases to suppress hydrocarbon production and promote the

60   formation of oxygenated products.[18-19]

61   While it is clear that adding silver influences the CO$_2$RR product distribution of

62   copper, the experimental observations on the CuAg systems were often conflicting: whereas

63   some enhanced the Faradaic efficiencies of both ethylene and ethanol,[25] some showed

64   enhancement only for ethylene,[22-23] while others improved the ethanol selectivity while

65   suppressing ethylene.[17, 21] Furthermore, despite commendable efforts in demonstrating the

66   CO-spillover phenomenon from Ag to Cu, there still remains a gap in understanding how the

67   CO that spilled over or migrated from the Ag sites may lead to the observed selectivity.[26-27] All

68 this suggests that the atomic-scale configuration of CuAg catalysts strongly determines their

69 CO_2RR product distribution, and calls for detailed mechanistic studies.

70 Herein, we probe the CO_2RR catalytic activity of a series of composite catalysts

71 consisting of Ag particles and oxide-derived Cu nanowires (OD-Cu NW). We assessed the

72 impact of increasing the amount of CO in the system on ethanol and ethylene production during

73 CO_2RR, and supplemented our analysis with density functional theory (DFT) calculations. Our

74 results indicate that at CuAg boundaries, an alternative pathway that allows the selective

75 production of ethanol is open. Interestingly, the pathway remains locked when CO is not

76 profusely evolved, indicating that CO availability is a key parameter to modulate the selectivity

77 of copper catalysts.

78 **2   Results and discussion**

79 **2.1   Materials Characterisation**

80 We synthesised Cu_2O nanowires using a published procedure.[28] Scanning electron

81 microscopy (SEM) revealed that these had diameters of 50-100 nm, and lengths of tens of

82 micrometers (Figure 1a). SEM and transmission electron microscopy (TEM) analyses of the

83 Ag powder (used as purchased) showed ~20 nm-sized particles (Figure 1b).

84 The Cu_2O nanowires and 20 nm Ag powders were physically mixed as a catalyst ink

85 and drop-casted onto graphite substrates (see the Supporting Information, SI, Section S1). We

86 labelled the composite catalyst as $Cu(Ag-D)_M$, where D is the diameter (in nanometers) of the

87 Ag particles and M is the nominal molar ratio of Ag/Cu. The SEM image of as-prepared

88 $Cu(Ag-20)_{20}$ shows that the Cu_2O nanowires and Ag particles were well mixed (Figure 1c),

89 confirmed by elemental mapping from energy-dispersive X-ray spectroscopy (EDX; Figure 1d,

90 e). The morphologies of all these materials did not change significantly after they were used

91 as catalysts for one hour CO_2RR in 0.1 M $KHCO_3$ electrolyte at a representative potential

of -1.1 V vs RHE (reversible hydrogen electrode; all potentials hereafter are referenced to the RHE; Figure 1f to j). EDX analysis indicates that after electrolysis, the Ag/Cu ratio of $Cu(Ag-20)_{20}$ increased from 18 ± 2 to 22 ± 2 (SI Section S2.1). This suggests that some Cu dissolution might have occurred.
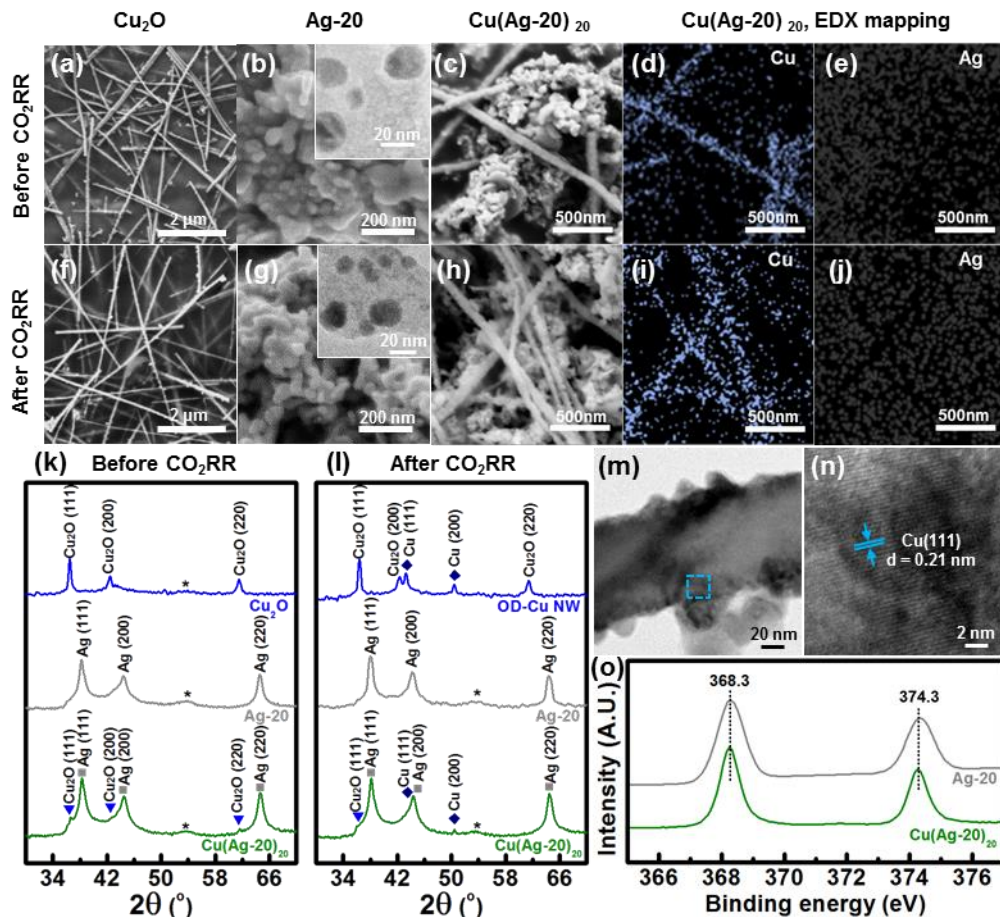
Figure 1. SEM images of as-prepared (a) Cu_2O nanowires (b) Ag-20, (c) $Cu(Ag-20)_{20}$ composite catalysts. (d) and (e) are respectively the Cu and Ag EDX maps of $Cu(Ag-20)_{20}$. (f)-(j) are the SEM images and EDX maps of the catalysts after one hour of CO_2 reduction at -1.1 V vs RHE. TEM images of Ag-20 are shown in the inserts of (b) and (g). XRD patterns of Cu_2O (blue lines), Ag-20 (grey lines) and $Cu(Ag-20)_{20}$ (green lines) (k) before and (l) after one hour of CO_2 reduction at -1.1 V vs RHE. The peaks are assigned using standard XRD patterns JCPDS 01-071-3645(Cu_2O), JCPDS 01-070-3038 (Cu) and 03-065-8428 (Ag). We note that Cu (111) and Ag (200) peaks overlap. Peaks from the graphite substrate are indicated with *. (m) TEM image of OD-Cu NW after CO_2 reduction at -1.1V vs RHE. (n) HRTEM analysis of OD-Cu NW after electrolysis. The analysis region is indicated in blue on Figure 1m. (o) Ag 3d XPS spectra of Ag-20 and $Cu(Ag-20)_{20}$ after CO_2 reduction at -1.1V vs RHE.

107   The identities of the as-prepared catalysts were confirmed by X-ray diffraction (XRD)

108   (Figure 1k). Ag peaks dominated the diffraction pattern of $Cu(Ag-20)_{20}$, due to its high Ag

109   content. After electrolysis, both metallic Cu (with Cu(111) as the strongest peak) and Cu_2O

110   signals were observed on OD-Cu NW (Figure 1l). TEM analysis of the OD-Cu NW (Figure

111   1m, n) after electrolysis confirms that its surface was reduced to metallic Cu. This observation

112   is consistent with previous works which showed that the surface of copper oxides was reduced

113   to metallic Cu under CO_2 reduction conditions.[5, 29-30] Both Cu and Cu_2O signals were also

114   observed in the XRD pattern of $Cu(Ag-20)_{20}$ after one hour of CO_2 electrolysis (Figure 1l).

115   TEM analysis of post-reduced $Cu(Ag-20)_{20}$ confirms that, similar to OD-Cu NW, the surface

116   of the Cu_2O nanowires in the composite catalyst was reduced to metallic Cu (Figure S1b).

117   It is noteworthy that $Cu(Ag-20)_{20}$, both before and after electrolysis, did not exhibit

118   XRD peaks that could be assigned to CuAg alloys. This observation is consistent with Cu and

119   Ag being immiscible in the solid state.[31] Furthermore, TEM analysis of $Cu(Ag-20)_{20}$ after

120   electrolysis revealed that the Ag particles were not strongly adhered to the OD-Cu NW, and

121   that the OD-Cu NW surface consisted of only metallic Cu and was not incorporated with Ag

122   (Section S2.2). X-ray photoelectron spectroscopy was also performed on $Cu(Ag-20)_{20}$ and

123   Ag-20, after they were used for CO_2RR. The Ag_{3d} peaks of both catalysts exhibited the same

124   binding energies at 368.3 and 374.3 eV, which can be assigned to metallic Ag^0 (Figure 1o).[32]

125   This observation is consistent with the metallic Ag peaks observed in the XRD of both catalysts

126   (Figure 1l) and the pure Ag phase (no Cu incorporated) observed in the TEM analysis of post-

127   electrolysed $Cu(Ag-20)_{20}$ (Figure S1d). Collectively, these evidences demonstrate that the Cu

128   and Ag phases in $Cu(Ag-20)_{20}$ are segregated, and they do not modify each other electronically.

129   This important piece of information will be used later to devise the DFT calculations.

130

2.2 CO_2RR activity of OD-Cu NW, Ag-20 particles and Cu(Ag-20)$_{20}$ composites

The CO_2RR activities of oxide-derived Cu nanowires (OD-Cu NW), Ag-20 particles, Cu(Ag-20)$_{20}$ catalysts were evaluated using chronoamperometry from -0.9 to -1.2 V vs RHE in 0.1 M $KHCO_3$ electrolytes (SI Section S3). The CO_2RR product distributions are presented in Figure 2a-c and Section S3 of the SI.

On OD-Cu NW, the optimal FEs of ethanol and ethylene were 7.3% and 20.1% respectively at -1.1 V ($FE_{ethanol}/FE_{ethylene}$ = 0.4; Figure 2a and Table S4). Methane became the dominant CO_2RR product (FE = 20.1% at -1.2 V) as more negative potentials were applied. Ag-20 reduced CO_2 to CO with FE of 80-90 % from -0.9 to -1.1 V (Figure 2b and Table S5). At -1.2 V, FE_{CO} decreased significantly to 68.1%, while FE_{H2} increased to 14.7% (Table S5), indicating that CO_2 mass transport limitations to the working electrode had occurred. We also detected minute amounts of methane (FE < 0.3%) and ethanol (FE < 0.4%) on Ag-20. This finding is consistent with earlier experimental and theoretical CO_2 electroreduction studies on Ag foils.[33-34]

On Cu(Ag-20)$_{20}$, CO_2RR to ethanol and ethylene peaked at -1.1 V, with FEs of 16.5 and 14.9 % respectively ($FE_{ethanol}/FE_{ethylene}$ = 1.1; Figure 2c and Table S6). The increase in $FE_{ethanol}/FE_{ethylene}$ from 0.4 to 1.1 indicates that the addition of Ag to OD-Cu NW enhances the selectivity of the composite catalyst towards ethanol. Note that control CO_2 electrolyses on pristine graphite substrates produced mainly H_2 (71 to 79% FE), some HCOOH (FE < 17%) and CO (FE < 4.1%) (Table S7). Neither hydrocarbons nor alcohols were detected.
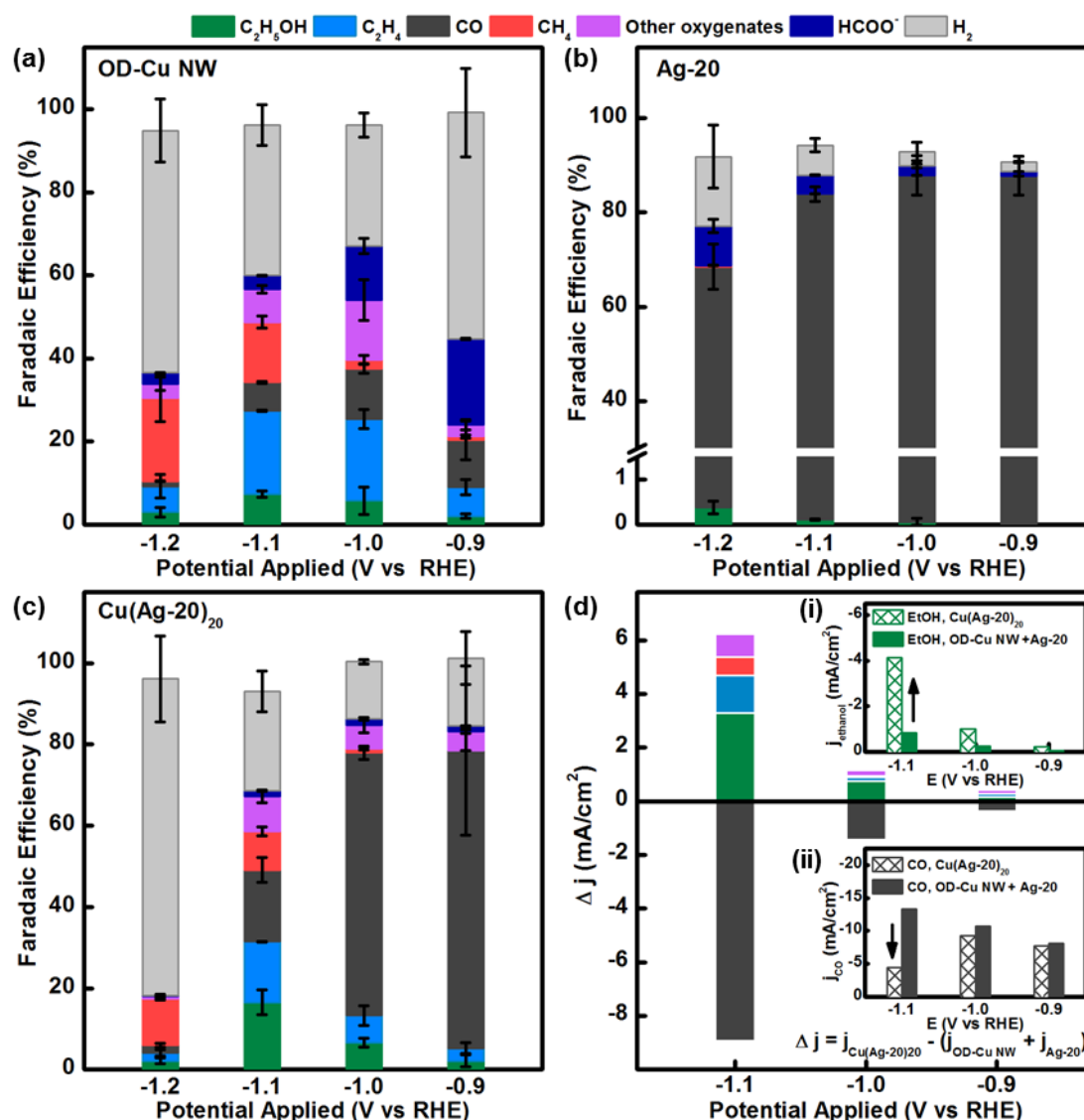
Figure 2. Faradaic efficiencies of CO_2 electrolysis products on (a) OD-Cu NW, (b) Ag-20 and (c) Cu(Ag-20)$_{20}$. (d) Difference in partial current densities ($\Delta j = j_{Cu(Ag-20)20} - (j_{OD-Cu\ NW} + j_{Ag-20})$) of major CO_2RR products formed on Cu(Ag-20)$_{20}$ and on OD-Cu + Ag-20. The other oxygenates include acetaldehyde, n-propanol, propionaldehyde, methanol and allyl alcohol. The inserts show the partial current densities of (i) ethanol and (ii) CO on Cu(Ag-20)$_{20}$ compared to the partial current densities from OD-Cu NW + Ag-20.

We also evaluate the difference in the geometric partial current densities ($\Delta j = j_{Cu(Ag-20)20} - (j_{OD-Cu\ NW} + j_{Ag-20})$) of major CO_2RR products formed on Cu(Ag-20)$_{20}$ and its two components (Figure 2d). Methane, ethylene, ethanol and other oxygenates (excluding formic acid) showed a positive Δj, with ethanol exhibiting the greatest value of Δj. Specifically, at -1.1 V, the $j_{ethanol}$ on OD-Cu NW + Ag-20 and Cu(Ag-20)$_{20}$ were -0.87 and -4.14 mA/cm^2 respectively, representing a nearly five-fold change (Figure 2d insert (i), SI Section S3). In

163   contrast, $j_{ethylene}$ and $j_{methane}$ increased by less than a factor of 1.6 from -2.35 to -3.76 mA/cm^2,

164   and -1.73 to -2.39 mA/cm^2 respectively (SI Section S3). CO had a negative Δj, with the largest

165   change also observed at -1.1 V (Figure 2d and insert (ii)). These observations suggest that on

166   the Cu(Ag-20)$_{20}$ catalyst, CO produced at Ag sites could have been consumed at other sites to

167   yield more reduced products, especially ethanol.

168   The stability of Cu(Ag-20)$_{20}$ was evaluated over five hours (SI Section S4). We observed

169   that the FEs of ethanol and ethylene decreased slightly from 16.4 to 12.2% and 13.4 to 11.0%,

170   respectively, while the FE_{CO} increased from 27.5% to 41.4%. Inductively coupled plasma-

171   optical emission spectrometry (ICP-OES) analysis detected only 0.1 ppm Cu (and no Ag) in

172   the used electrolyte, indicating Cu dissolution. EDX analysis of Cu(Ag-20)$_{20}$ after the

173   electrolysis showed that the Ag/Cu ratio had increased to 26±5 (Table S8). EDX mapping

174   reveals that some of the dissolved Cu had re-deposited as nanoparticles onto the catalyst surface

175   (Figure S3), which is consistent with structural changes expected from the dissolution-

176   redeposition processes on Cu.[4] These findings indicate that the Cu catalysts partially dissolved

177   during CO$_2$ electrolysis, which resulted in less Cu catalytic sites for the conversion of CO to

178   C$_2$ molecules. Consequently, ethylene and ethanol formation concurrently decreased, while

179   more CO (produced on Ag) was detected. Interestingly, $FE_{ethanol}/FE_{ethylene}$ remained stable at

180   about 1.1-1.2 across the five-hour duration of the experiment (Figure S2). This observation

181   suggests that, rather than the catalyst structure, the presence of CO is the main factor

182   influencing the $FE_{ethanol}/FE_{ethylene}$.

183   To sum up, we observe that more C$_2$ molecules were produced from the Cu(Ag-20)$_{20}$

184   composite than on OD-Cu, due to the utilization of CO molecules produced from the Ag sites.

185   Ethanol was the most enhanced product from this CO utilisation process.

2.3 Effect of Increased CO Production and Abundance of CuAg Boundaries

187   The analysis in the preceding section indicates that among the CO_2RR products, ethanol

188 benefits the most from the CO produced at Ag sites. Thus, we systematically studied how its

189 production might be impacted by the amount of CO introduced into the catalytic system.
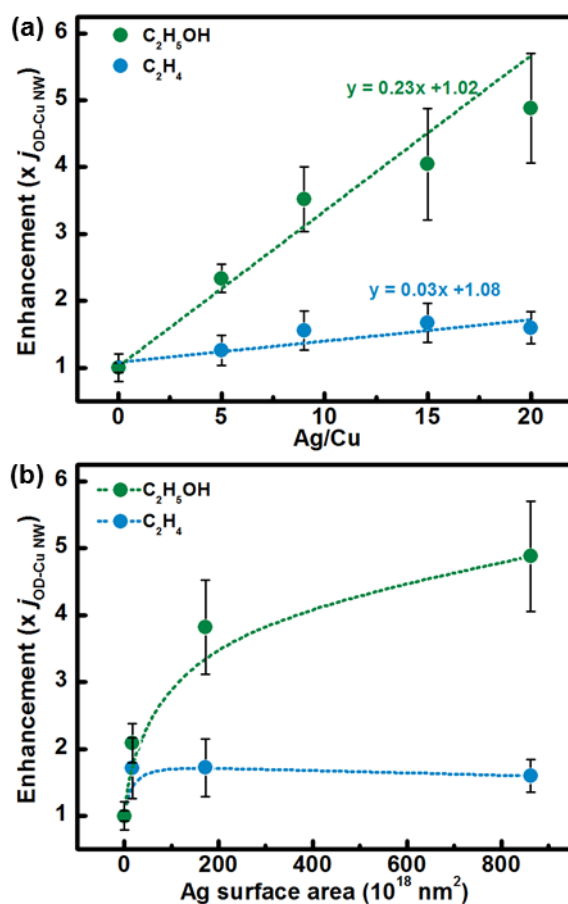
190 **Figure 3.** Dependence of ethanol and ethylene enhancement during CO_2 reduction at -1.1 V vs
191 RHE on (a) Ag/Cu ratio and (b) total Ag surface area (dashed lines are included as a guide to
192 the eye).

193

194   During CO_2RR, the amount of CO produced can be modulated by the loading of Ag

195 particles in the catalyst. Composites with Ag/Cu mole ratios of 5, 9 and 15 were prepared

196 (Figures S4 and S5, Table S9). The loading of Cu in all composites was kept constant, so that

197 the Ag/Cu ratios increased because of the progressive addition of Ag. CO_2RR was performed

198 at -1.1 V and ethanol enhancement was evaluated by normalising $j_{ethanol}$ from the CuAg

199 composites by $j_{ethanol}$ from OD-Cu NW (Table S10-S12). Ethylene enhancement was

200   determined analogously. We found that ethanol enhancement strongly correlates with Ag/Cu,

201   reaching a value of ~5 when Ag/Cu = 20 (i.e. the most Ag-rich sample; Figure 3a). In contrast,

202   the enhancement of ethylene was smaller, having a maximum value of 1.6. The slope of ethanol

203   enhancement against Ag/Cu was ~8 times larger than the slope for ethylene enhancement,

204   which suggests that ethanol production is appreciably more sensitive to the presence of CO, as

205   compared to ethylene production.

206   Recent theoretical and experimental works on CuAg catalysts have suggested that CO

207   produced on Ag sites can diffuse to Cu sites and be further reduced to C_1-C_3 products.[26, 35] We

208   hypothesized that this migration can be facilitated by increasing the amount of adjacent CuAg

209   sites. To test this, we performed CO_2RR at -1.1 V on Cu(Ag-100)$_{20}$ and Cu(Ag-1000)$_{20}$. These

210   two composites were prepared by mixing Cu_2O nanowires with either 100 nm or 1000 nm

211   diameter Ag particles (SI Section S6). With a constant Ag loading, the use of larger Ag particles

212   decreases the total Ag surface area in the CuAg composites. This, in turn, decreases the

213   abundance of adjacent Cu-Ag sites. Although the Ag particles studied have different sizes (20

214   to 1000 nm), they reduced CO_2 to CO with similar partial current densities between -9.5 to -

215   13.2 mA/cm^2 at -1.1V (Tables S5, 16 and 17). The ethanol and ethylene enhancement plotted

216   against the total surface area of Ag particles shows that ethanol production significantly

217   increases with Ag surface area. When the latter was increased by a factor of 50, the ethanol

218   enhancement increased from 2 to 5 (Figure 3b). In contrast, ethylene production did not show

219   a sizable increase. Thus, increasing the size of CuAg boundaries favours the production of

220   ethanol, but not ethylene.

221   We have also prepared a Cu(Ag-20)$_{20}$-S sample, which contained the same Cu and Ag

222   loading as Cu(Ag-20)$_{20}$, but had the Cu_2O and Ag components coated sequentially onto the

223   working electrode (SI Section S7). SEM analysis of this poorly-mixed catalyst clearly reveals

224   a lowering of the density of Cu-Ag boundaries. CO_2RR on this sample yielded ~30% higher

225   j_{CO}, but less than 50% $j_{ethanol}$ than that observed on $Cu(Ag-20)_{20}$ (Figure S7, Table S18). This

226   shows that when the CuAg contact area is decreased, CO migrates less efficiently to the Cu

227   sites for further reaction to form ethanol. Further control experiments performed on Ag

228   nanoclusters galvanically deposited onto electropolished Cu foils also show that the

229   enhancement of ethanol was affected more significantly than ethylene by the length of CuAg

230   boundaries (Section S8).

231   Some studies suggest that oxide-derived copper differs from metallic copper catalysts

232   due to the presence of residual oxides, which improve *CO binding, and facilitate C-C

233   coupling.[36-37] However, others maintain that metallic copper is the active catalyst in oxide-

234   derived copper because residual oxides are unstable and inactive for catalysis under CO_2RR

235   conditions.[30, 38-39] In view of this contention, we prepared a $Cu(Ag-20)_{20}$-M composite, which

236   consisted of metallic Cu nanowires (Cu NW) well-mixed with Ag-20 (SI Section S9). CO_2RR

237   at -1.1 V on $Cu(Ag-20)_{20}$-M revealed that, compared to Cu NW, $j_{ethanol}$ had increased 20 times,

238   while $j_{ethylene}$ increased 4 times. This shows that the ethanol-selective enhancement due to the

239   presence of CO is not unique to oxide-derived Cu surfaces, but also applies to metallic Cu

240   surfaces.

241   Since our results hint towards the importance of CO in enhancing ethanol production,

242   we electroreduced CO directly on OD-Cu NW and $Cu(Ag-20)_{20}$ at -0.75, -0.80 and -0.90V (SI

243   Section S10). Unexpectedly, in this potential range, $FE_{ethylene}$ was higher than $FE_{ethanol}$ on both

244   OD-Cu NW and $Cu(Ag-20)_{20}$. We hypothesized that this apparent discrepancy could be due to

245   the lack of CO reactants at the electrode, when it is operating at high current densities. To

246   assess this hypothesis, we estimate using Fick's law that the flux of CO reaching the electrode

247   during electrolysis is ~2.0 nmol cm^{-2} s^{-1} (SI Section S10.1). This value is about one order of

248   magnitude smaller than the 68 nmol cm^{-2} s^{-1} of CO generated in-situ by Ag sites in the

249   composite during CO_2RR at -1.1 V, i.e. the potential where we observed the largest

250   enhancement of ethanol on $Cu(Ag-20)_{20}$ (SI Section S10.2). Our calculations show that under

251   CO reduction conditions at -0.75 to -0.9 V, there is insufficient CO to enable selective ethanol

252   production. During CO_2RR, therefore, a CO-selective co-catalyst in tandem with Cu is crucial

253   to provide a large enough flux of CO for further reduction to ethanol.

254   Unlike several previously-reported CuAg catalysts, the formation of hydrocarbons on

255   the present CuAg composites was not suppressed in favour of enhanced ethanol production.[17,]

256   [19] We attribute this to the clear phase separation between copper and silver sites in our

257   composites (Figure 1). This differs from the catalysts studied in earlier works, which showed

258   miscibility between those two metals.[17, 19] These catalysts were prepared by targeted

259   procedures such as the use of complexing agents[17] and electron-beam physical vapour

260   deposition,[19] so as to preserve the metastable CuAg miscibility. Mixed-phase catalysts have

261   been suggested to be less oxophilic and thus exhibit a higher propensity for suppressing

262   hydrocarbon production.[18-19] Furthermore, recent isotope-labelling studies of CO_2RR on oxide-

263   derived copper suggested the presence of distinctively different catalytic sites for ethanol and

264   ethylene production.[40] This is in line with our experimental observation regarding ethanol

265   enhancement and the idea that the selective electroreduction of CO_2 to ethanol can occur on

266   active sites different from those for *CO dimerisation, which mainly produces ethylene.

267   **2.4   Computational modelling of CO_2RR at CuAg boundaries**

268   To understand in greater detail the working principle of the CuAg catalysts, we

269   performed Density Functional Theory (DFT) calculations on model systems. First, to decide

270   on the characteristics of the model system, we calculated the thermodynamic stability of bulk

271   Cu-Ag alloys for different Cu/Ag proportions. Bulk Cu-Au alloys, which have been extensively

272   studied,[41-42] were also analysed as a control system. For the latter, we find that the alloy

273   formation energy is negative for all the studied proportions, in line with experimental results

274   from the literature.[41-42] Conversely, for the CuAg system, the alloy formation energies were

275   positive in all cases, indicating that it is not thermodynamically favourable to alloy Cu and Ag

276   in any of the studied proportions (Figure S11). This leads us to conclude that Ag and Cu likely

277   exist as two separated phases in our catalyst, which is also supported by the characterisation

278   results of our CuAg composite catalyst.

279   In view of the current controversy regarding the presence of oxygen on oxide-derived Cu

280   electrodes,[37-39] we performed calculations featuring surface and subsurface oxygen on both

281   Cu(111) and Ag(111) (Table S30). We observe that while subsurface oxygen is metastable on

282   both metals, surface oxygen is more stable by 1.5 and 0.7 eV, respectively. In view of its low

283   stability and negligible effect on the adsorption energies of *CO, we did not include subsurface

284   *O in our model. Neither did we include the effects of surface *O in our calculations as

285   previous works have shown that it is unlikely for surface *O to be present on Cu and Ag

286   surfaces when they are subjected to the negative potentials needed for electrochemical

287   CO_2RR.[43-44]

288   After outlining the model systems, we performed a mechanistic study. For clarity, we

289   divided the entire CO_2RR to ethanol, which requires twelve proton-electron transfers ($2CO_2$ +

290    $12(H^+ + e^-) \rightarrow CH_3CH_2OH + 3H_2O$), into three separate yet interconnected parts. First, we

291   consider the reduction of two CO_2 molecules to 2*CO, where four protons and electrons are

292   transferred. This is followed by the reduction of 2*CO to *CHCO, which takes three proton-

293   electron transfers and a C-C coupling. Finally, we close the analysis with *CHCO reduction to

294   ethanol, where five protons and electrons are transferred.

295   CO_2RR to CO via *COOH was studied on Cu(111) (copper's closest-packed surface), a

296   Ag cluster on top of Cu(111) (hereon referred to as Ag@Cu, see the insert of Figure 4a), and

297   Cu(211), which is composed of (111) terraces separated by (100) steps. Cu(211) is chosen

298   because models based on its step edge sites reproduce well the experimental features of CO_2RR

299   to C_1 and C_2 products.[45-46] On Cu(111) and Cu(211), the desorption of *CO to $CO_{(g)}$ is not

300   favourable (Figure 4a). Hence, *CO will further reduce to CH_x species at negative enough

301   potentials, eventually leading to CH_4.[45] In contrast, Ag@Cu sites reduce CO_2 to *CO, which is

302   so weakly adsorbed on Ag that it cannot undergo further reduction. Thus, these *CO will either

303   diffuse into the solution or migrate to neighbouring Cu sites. The vertical differences in Figure

304   4a indicate that *CO is stabilized by 0.11 eV upon desorption from Ag to the solution, whereas

305   it is stabilized by 0.39 eV when it migrates to the Cu(111) surface. The kinetic barrier for *CO

306   diffusion from the Ag cluster to Cu(111) is only 0.17 eV (Table S29), which is easily

307   surmountable at room temperature (surmountable barriers are typically below 0.75 eV).[47]

308   Because of their strong adsorption energies, the Cu(211) step-edge sites are probably covered

309   by reaction intermediates irrespective of *CO abundance. In contrast, the coverage of reaction

310   intermediates at weakly-adsorbing Cu(111) sites remains relatively low when there is no excess

311   *CO. Thus, we postulate that ethanol evolves from Cu(111) sites near Ag nanoparticles. This

312   implies that CuAg boundaries are dual active sites, in that $CO_{(g)}$ formed at Ag particles diffuses

313   to unoccupied Cu(111) sites, where it is then further reduced.
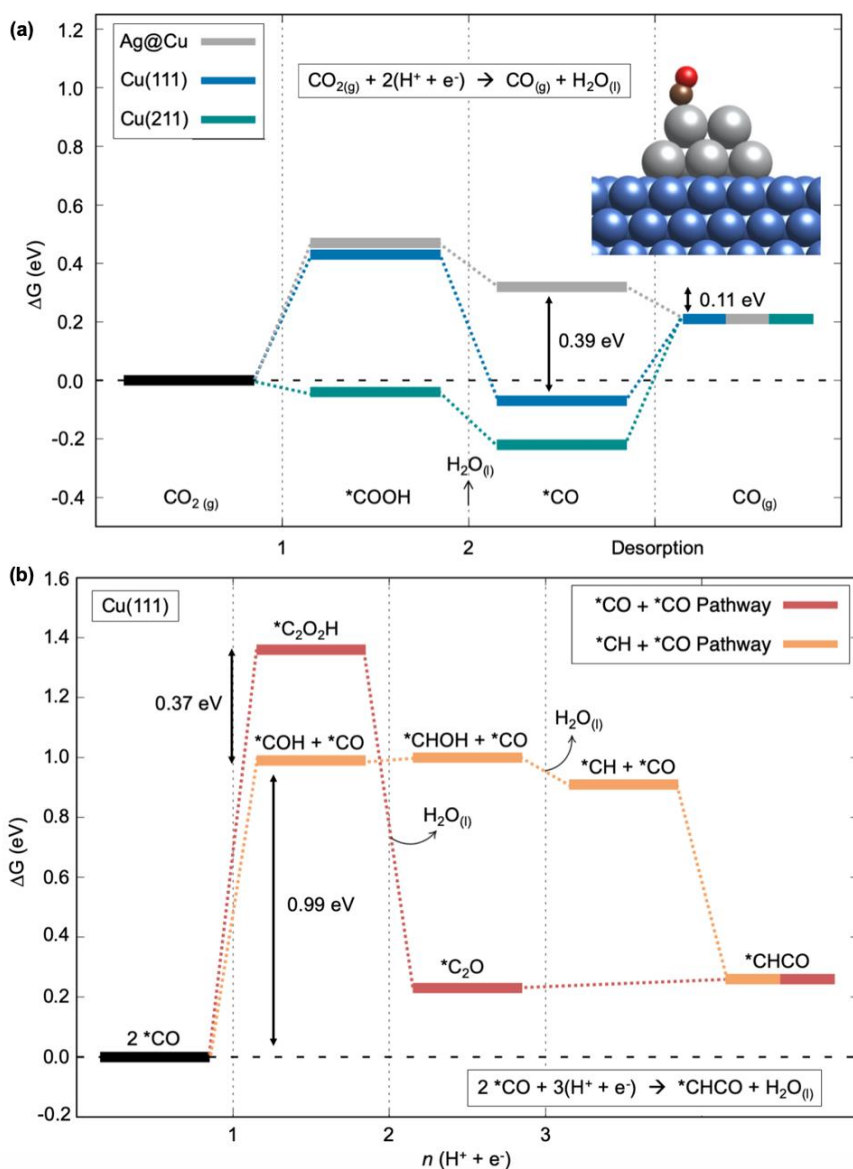
Figure 4. a) Free energy diagram of $CO_{2(g)}$ electroreduction to $CO_{(g)}$ on Cu(111) (blue), Cu(211) (cyan), and Ag@Cu (grey), which is a Ag cluster on top of a Cu(111) slab. All energies are referenced to CO_2 and proton-electron pairs. Insert: CO adsorbed on the Ag@Cu cluster; Cu, Ag, C, and O atoms are shown in blue, grey, brown and red, respectively. b) Free energy diagram on Cu(111) featuring two different C-C coupling pathways to *CHCO from 2*CO. In red, the *CO dimerisation pathway. In orange, the energetics of the *CH + *CO pathway. All energies are referenced to 2*CO adsorbed on Cu(111) and proton-electron pairs, see section S15.

As shown in Figure 4b, the reduction of 2*CO to C_2 species can proceed in two ways, namely through the conventional CO dimerisation pathway, or via the coupling of *CO and CH_x species. To ascertain the actual species which are likely to couple with CO to produce ethanol, we calculated several coupling barriers on Cu(111). A summary of all values obtained

327   for the different coupling reactions can be found in Section S15 of the SI. For *CH + *CO (x

328   = 1), *CH$_2$ + *CO (x = 2), and *CH$_3$ + *CO (x = 3) through a Langmuir-Hinshelwood (L-H)

329   mechanism on Cu(111), we obtained barriers of 0.70, 0.71, and 1.20 eV, respectively, which

330   are commensurate with those in the literature.[48] Earlier studies have also suggested an Eley-

331   Rideal (E-R) mechanism for the coupling of CO and CH$_x$.[15-17, 49] To assess this possibility, we

332   calculated the energy barriers of the *CH + CO$_{(g)}$ and *CH$_2$ + CO$_{(g)}$ couplings via an E-R

333   mechanism. The respectively obtained values are 1.40 and 1.49 eV, which are appreciably

334   higher than the L-H values on Cu(111). Judging by all of the calculated barrier heights, the

335   reaction may proceed through L-H routes coupling *CH and *CO, or *CH$_2$ and *CO, but not

336   between *CH$_3$ and *CO. Note that while we calculated coupling and diffusion barriers, we did

337   not perform calculations of proton-electron transfer barriers, since, as noted recently by

338   Rossmeisl et al,[50] there is 'not (yet) a method to obtain electrochemical barriers between

339   realistic states at constant electrochemical conditions'. We further note that other authors have

340   extensively studied the Brønsted-Evans-Polanyi (BEP) relations for reactions where C, H and

341   O-containing species are involved, and have shown that thermodynamics and kinetics are

342   generally well correlated for such reactions on transition metal surfaces.[51-52]

343   Figure 4b shows that, in terms of the potential-limiting step (i.e. *CO hydrogenation), the

344   *CH + *CO coupling pathway is more favourable than that of CO dimerisation on Cu(111) by

345   ~0.37 eV. This means that *CO is likely reduced to *COH on Cu(111), and not to its

346   hydrogenated dimer *C$_2$O$_2$H. On Cu(111) without any vicinal Ag nanoparticles, this preference

347   has two justifications: (1) the low coverage makes it statistically difficult for *CO to couple,

348   and (2) the thermodynamics and kinetics of CO dimerisation are energetically prohibitive. If

349   and when *CO is abundant on Cu(111), (1) is solved but (2) is not, so that the coupling likely

350   takes place between *CH and *CO, or *CH$_2$ and *CO. In agreement with experiments, Figure

351   4b indicates that opening the *CH + *CO pathway requires potentials of at least -0.99 V vs

RHE (we explain how to calculate limiting potentials from free energies in Section 4:

353 Computational Details).
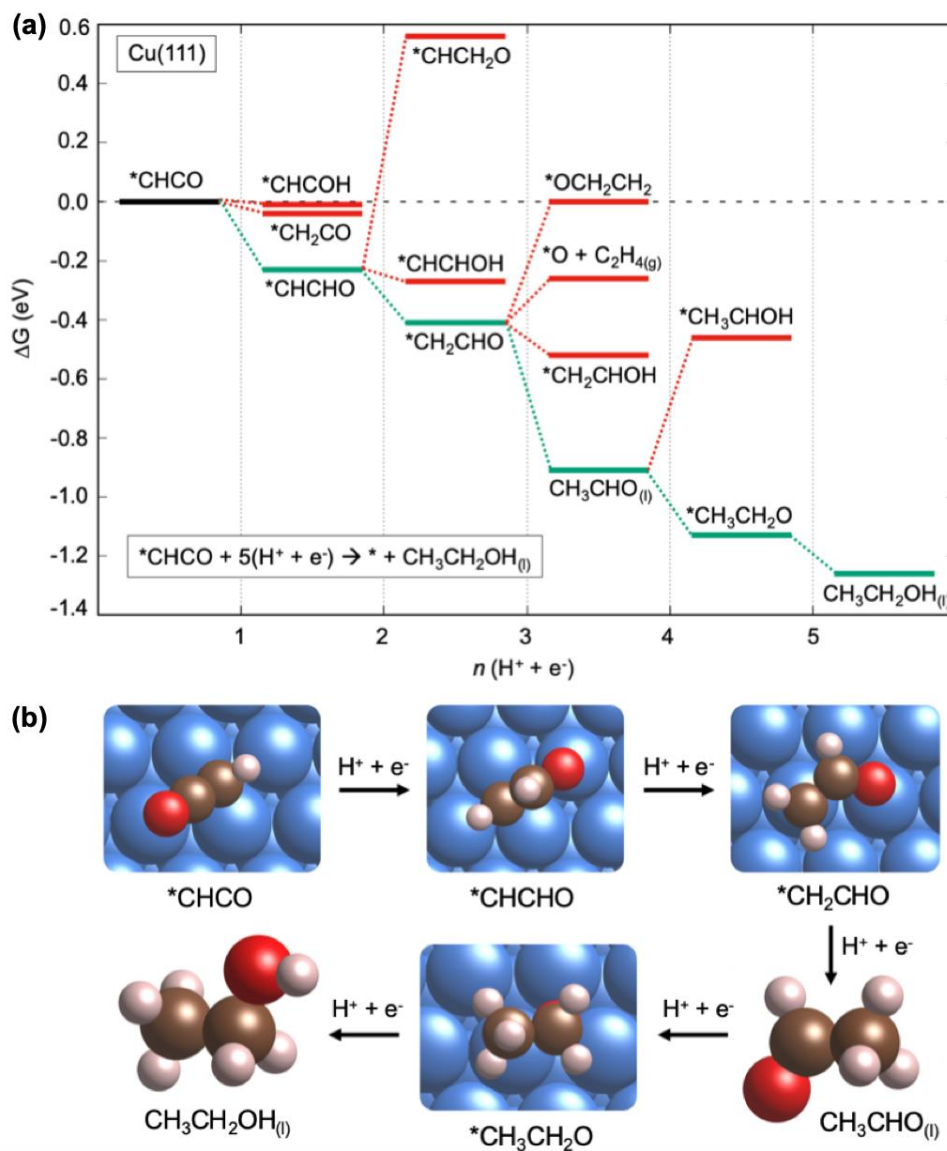
Figure 5. Reduction of CH_xCO to ethanol on Cu sites. a) Free energy diagram of the electroreduction of *CHCO and *CH_2CO on Cu(111). The preferred pathway is shown in green, whereas less stable intermediates are shown in red. Note that ethylene production is considerably less favourable than that of ethanol. All energies are referenced to *CHCO and proton-electron pairs, see Section S15. b) Atomic structures of the species in the *CHCO preferred electroreduction pathway. Cu, C, O, and H atoms are shown in blue, brown, red, and white.

362 Finally, we studied the fate of the *CHCO moieties upon further reduction (Figure 5). The

363 most favourable reduction pathway to ethanol is coloured in green in Figure 5a, whereas less

364 favourable species are displayed in red at each stage of the reaction. For convenience, the

365 atomic structures of the most favourable reduction path are depicted in Figure 5b. A more

366 extended analysis, including the further reduction of $*CH_2CO$ and $*CH_3CO$ species is depicted

367 in Figure S10. It is striking that regardless of whether $*CHCO$ or $*CH_2CO$ is the result of the

368 coupling step, the pathway always inclines towards ethanol, instead of ethylene. The same

369 holds for $*CH_3CO$. This leads to a simple conclusion: once $*CO + *CH_x$ coupling takes place

370 on CuAg catalysts, ethanol is selectively produced. This is consistent with our experimental

371 findings (Figure 3), wherein enhanced CO availability increases ethanol production. This is

372 also supported by our results from using $Cu(Ag-20)_{20}$ for the electroreduction of acetaldehyde

373 (Section S11), an isolable intermediate in our proposed mechanism. Ethanol was the major

374 reduction product, while ethylene was not detected. Besides, several previous theoretical and

375 experimental studies have shown that acetaldehyde is a precursor of ethanol.[9, 12, 15, 53] This result

376 also helped us to exclude a previously proposed pathway implicating solvent water as the

377 oxygen source for ethanol.[54] In that mechanism, ethanol production did not proceed via

378 acetaldehyde, and the pathway with the lowest energy barrier leads to ethylene formation.

379 In summary, bare Cu(111) terraces are relatively inactive for the production of C_2

380 molecules, in view of the low $*CO$ coverage and the comparatively easier formation of C_1

381 adsorbed species.[55-56] However, the calculations in Figures 4 and 5 show that abundant $*CO$

382 facilitates the formation of C-C bonds at Cu(111) terraces and the selective formation of

383 ethanol, without the energy-intensive formation of CO dimers.[11, 55, 57]

384 **3   Conclusion**

385 A series of CuAg composites shows enhanced selective CO_2 reduction towards ethanol. A

386 fivefold improvement in $j_{ethanol}$ was observed on an optimised $Cu(Ag-20)_{20}$ sample (-4.1

387 mA/cm^2; compared to $-0.85 mA/cm^2$ on OD-Cu NW). In contrast, $j_{ethylene}$ only increased slightly

388 by a factor of ~1.6. These observations indicate the opening of a second pathway to reduce

389   CO_2 selectively to ethanol, which is likely activated in excess of *CO. Unlike ethylene

390   production, which is usually thought to proceed via *CO dimerisation, the alternative pathway

391   proceeds via *CO + *CH_x (x = 1, 2) coupling at CuAg boundaries, and the formed *CH_xCO

392   species are in all cases shown to preferably reduce to ethanol.

393   In a broader context, our work hints towards the fact that certain sites at catalytic surfaces

394   are usually inactive because of their inability to stabilize particular adsorbate(s). If and when a

395   workaround is found, catalytic activity and selectivity can be sizably enhanced. This is the case

396   of Cu(111) sites, on which it is typically hard to produce C_2 molecules but, in excess of *CO,

397   are able to reduce CO_2 selectively to ethanol. We hope this rationale opens up new possibilities

398   in designing electrocatalysts with enhanced product selectivities for CO_2 reduction.

399   **4   Methods**

400   <u>Synthesis of Cu_2O nanowires.</u> 120 μL of o-anisidine (Aldrich) were added to 60 mL of

401   deionised water containing 0.3 g of copper (II) acetate monohydrate (Sigma-Aldrich). The

402   solution was stirred for 5 min until its colour turned olive green. It was then transferred into a

403   stainless steel autoclave and heated at 200 °C for 14 hours to yield Cu_2O nanowires. The

404   product was decanted, washed with ethanol and dried in the oven at 60 °C overnight.[28]

405   <u>Preparation of Cu(Ag-D)$_M$ composite catalysts.</u> Ag powders with diameters of 20 nm (US

406   Research Nanomaterials), 100 nm (American Elements) and 1000 nm (Goodfellow) were

407   purchased and used as received. The Cu-to-Ag ratios of the composite catalysts were controlled

408   by using different mass ratios of the Cu_2O nanowires and Ag powders, with the loading of

409   Cu_2O fixed at 1 mg (Table S1). The powders were dispersed in 1 mL of solvent (75% water,

410   15% ethanol, 10% Nafion) and sonicated until a homogenous ink was obtained. 25 μL of the

411   ink was drop-casted onto polished graphite discs (15 mm diameter, Ted Pella) and dried in air.

412 <u>Physical characterisation of catalysts.</u> Scanning electron microscopy and energy dispersive

413 X-ray spectroscopy were performed using a JEOL JSM-6701F SEM. Transmission electron

414 microscopy was performed using a JEOL 3010 TEM. The catalysts were removed from the

415 graphite substrates and dispersed in ~1mL methanol by sonication. 20μL of the dispersion was

416 drop-casted onto 300 mesh nickel grid coated with lacey carbon (LC325-Ni, Electron

417 Microscopy Sciences) for TEM analysis. Powder X-ray diffraction was made using a Siemens

418 5005 (CuKα radiation with graphite monochromator), in locked θ-2θ scan mode from 15 to

419 100° 2θ with 0.1° resolution step and 1 second acquisition time per step. X-ray photoelectron

420 spectroscopy analysis was performed using a Theta Probe (Thermo Scientific) XPS instrument

421 with a monochromatic Al Ka (1486.6 eV) X-ray source. The binding energies were calibrated

422 based on the C_{1s} peak at 285 eV.

423 <u>Electrochemical CO_2 reduction experiments.</u> Electrolyses (1 hr) were performed in 0.1 M

424 $KHCO_3$ (Merck, 99.7%), using a two compartment Teflon cell separated by an anion-exchange

425 membrane (Selemion AMV, AGC Asahi Glass). The cathode compartment contained 12 mL

426 of electrolyte and housed the working electrode (exposed geometric surface area: 0.785 cm^2)

427 and the reference electrode (Ag/AgCl saturated KCl, Pine), while the anode compartment

428 contained 8 mL of electrolyte and a graphite rod (Ted Pella) as counter-electrode. The

429 electrolyte was purged with CO_2 gas (99.999%, Linde Gas) at 20 cm^3/min. The pH of the

430 electrolyte was 6.8. The electrochemical measurements were performed using a Gamry

431 Reference 600 potentiostat/galvanostat. The current interrupt method was used to compensate

432 for the iR drop. The headspace of the cathode compartment was continuously flowed into a gas

433 chromatograph (GC, Agilent 7890A) for online detection of gas products. Liquid products were

434 analyzed after the electrolysis experiments. Aldehydes, ketones and alcohols were detected

435 using headspace GC (HSGC, Agilent, 7890B and 7697A). Formate and acetate were detected

436   using high performance liquid chromatography (Agilent 1260 Infinity) using an Aminex HPX-

437   87H column, variable wavelength detector, and 0.5 mM H_2SO_4 mobile phase.

438   <u>Computational details.</u> The DFT simulations were made with the VASP[58] code using the PBE

439   exchange-correlation functional[59] and the projector augmented-wave method.[60] Cu(111) was

440   modelled with a 3×3 supercell, and Cu(211) with a 3×1 one. All Cu slab models contained four

441   metal layers and were modelled with a lattice constant of 3.64 Å, typical of PBE. The topmost

442   two layers and the adsorbates were relaxed in all directions, while the bottommost layers were

443   fixed at the bulk equilibrium distances. CuAg boundaries were modelled with a 7-atom Ag

444   cluster (made of a layer of five atoms in contact with Cu and two Ag atoms on top of it) situated

445   in adjacent *fcc* hollows of a 4×4 supercell Cu(111) slab. Such slab size avoids lateral

446   interactions between Ag clusters. We used a plane-wave cutoff of 450 eV, k_BT = 0.2 eV

447   (extrapolating total energies to 0 K), and the conjugate-gradient optimization scheme until the

448   maximal force on any atom was below 0.05 eV Å^{-1}. Monkhorst-Pack meshes[61] of 4×4×1,

449   4×5×1, and 3×3×1 for Cu(111), Cu(211), and CuAg boundaries ensured convergence of the

450   adsorption energies within 0.05 eV. The distance between repeated images in the vertical

451   direction was larger than 16 Å and dipole corrections were applied. Isolated molecules were

452   calculated in boxes of 9 Å x 10 Å x 11 Å using k_BT = 0.001 eV and the gamma point.

453   The reaction free energies were approximated as $\Delta G \approx \Delta E_{DFT} + \Delta ZPE - T\Delta S +$

454    $\Delta E_{solvation}$, where ΔE_{DFT} is the DFT-calculated reaction energy, ΔZPE is the zero-point

455   energy change and $T\Delta S$ is the entropy change at 298.15 K. ΔS includes only the vibrational

456   entropy for the adsorbates and all the contributions for free molecules. The computational

457   hydrogen electrode was used to model proton-electron pairs. Solvation was modelled as an

458   external correction depending on the chemical nature of the adsorbates (specific values are

459   given in Table S25).[11, 62] Transition state geometries were found using the climbing image

460   nudged elastic band method,[63] ensuring that at the saddle point only one imaginary frequency

461   along the reaction coordinate was observed. In this case, the limiting potentials U_L were

462   calculated based on the largest positive free energies of reaction: $U_L = -\Delta G_{max}/e^-$, where e^-

463   is the magnitude of the charge of an electron.

464   Detailed information on gas-phase, liquid-phase, and solvation corrections; specific

465   values of adsorption free energies and kinetic energy barriers; and the optimized geometries

466   coordinates of all the calculations featured in this work can be found in the SI, Sections S12 to

467   S16.

468   **Supporting Information Available**

469   Catalyst loadings, physical characterisations and electrolysis data of all catalysts tested,

470   including electrolysis of intermediates. Gas-phase and liquid-phase corrections, solvent

471   contributions to free energies, adsorption energies, kinetic barriers and optimised geometries

472   used in DFT calculations. This information is available free of charge on the ACS Publications

473   website.

5   References

(1)   Lu, Q.; Jiao, F., Electrochemical CO_2 Reduction: Electrocatalyst, Reaction Mechanism, and Process Engineering. *Nano Energy* **2016,** *29*, 439-456.

(2)   Hori, Y.; Murata, A.; Takahashi, R., Formation of Hydrocarbons in the Electrochemical Reduction of Carbon Dioxide at a Copper Electrode in Aqueous Solution. *J. Chem. Soc. Faraday Trans. 1* **1989,** *85*, 2309-2326.

(3)   Kuhl, K. P.; Cave, E. R.; Abram, D. N.; Jaramillo, T. F., New Insights into the Electrochemical Reduction of Carbon Dioxide on Metallic Copper Surfaces. *Energy Environ. Sci.* **2012,** *5*, 7050-7059.

(4)   Handoko, A. D.; Ong, C. W.; Huang, Y.; Lee, Z. G.; Lin, L.; Panetti, G. B.; Yeo, B. S., Mechanistic Insights into the Selective Electroreduction of Carbon Dioxide to Ethylene on Cu_2O-Derived Copper Catalysts. *J. Phys. Chem. C* **2016,** *120*, 20058-20067.

(5)   Ren, D.; Deng, Y.; Handoko, A. D.; Chen, C. S.; Malkhandi, S.; Yeo, B. S., Selective Electrochemical Reduction of Carbon Dioxide to Ethylene and Ethanol on Copper (I) Oxide Catalysts. *ACS Catal.* **2015,** *5*, 2814-2821.

(6)   Lum, Y.; Yue, B.; Lobaccaro, P.; Bell, A. T.; Ager, J. W., Optimizing C-C Coupling on Oxide-Derived Copper Catalysts for Electrochemical CO_2 Reduction. *J. Phys. Chem. C* **2017,** *121*, 14191-14203.

(7)   Bushuyev, O. S.; De Luna, P.; Dinh, C. T.; Tao, L.; Saur, G.; van de Lagemaat, J.; Kelley, S. O.; Sargent, E. H., What Should We Make with CO_2 and How Can We Make It? *Joule* **2018,** *2*, 825-832.

(8)   Spurgeon, J. M.; Kumar, B., A Comparative Technoeconomic Analysis of Pathways for Commercial Electrochemical CO_2 Reduction to Liquid Products. *Energy Environ. Sci.* **2018,** *11*, 1536-1551.

(9)   Schouten, K. J. P.; Kwon, Y.; van der Ham, C. J. M.; Qin, Z.; Koper, M. T. M., A New Mechanism for the Selectivity to C_1 and C_2 Species in the Electrochemical Reduction of Carbon Dioxide on Copper Electrodes. *Chem. Sci.* **2011,** *2*, 1902-1909.

(10)   Gattrell, M.; Gupta, N.; Co, A., A Review of the Aqueous Electrochemical Reduction of CO_2 to Hydrocarbons at Copper. *J. Electroanal. Chem.* **2006,** *594*, 1-19.

(11)   Calle-Vallejo, F.; Koper, M. T. M., Theoretical Considerations on the Electroreduction of CO to C_2 Species on Cu(100) Electrodes. *Angew. Chem. Int. Ed.* **2013,** *52*, 7282-7285.

(12)   Bertheussen, E.; Verdaguer‑Casadevall, A.; Ravasio, D.; Montoya, J. H.; Trimarco, D. B.; Roy, C.; Meier, S.; Wendland, J.; Nørskov, J. K.; Stephens, I. E. L.; Chorkendorff, I., Acetaldehyde as an Intermediate in the Electroreduction of Carbon Monoxide to Ethanol on Oxide-Derived Copper. *Angew. Chem. Int. Ed.* **2015,** *55*, 1450-1454.

(13)   Ledezma-Yanez, I.; Gallent, E. P.; Koper, M. T. M.; Calle-Vallejo, F., Structure-Sensitive Electroreduction of Acetaldehyde to Ethanol on Copper and Its Mechanistic Implications for CO and CO_2 Reduction. *Catal. Today* **2016,** *262*, 90-94.

(14)   Murata, A.; Hori, Y., Product Selectivity Affected by Cationic Species in Electrochemical Reduction of CO_2 and CO at a Cu Electrode. *Bull. Chem. Soc. Jpn.* **1991,** *64*, 123-127.

(15)   Hori, Y.; Takahashi, R.; Yoshinami, Y.; Murata, A., Electrochemical Reduction of CO at a Copper Electrode. *J. Phys. Chem. B* **1997,** *101*, 7075-7081.

(16)   Ren, D.; Ang, B. S.-H.; Yeo, B. S., Tuning the Selectivity of Carbon Dioxide Electroreduction Toward Ethanol on Oxide-Derived Cu_xZn Catalysts. *ACS Catal.* **2016,** *6*, 8239-8247.

(17)   Lee, S.; Park, G.; Lee, J., Importance of Ag–Cu Biphasic Boundaries for Selective Electrochemical Reduction of CO_2 to Ethanol. *ACS Catal.* **2017,** *7*, 8594-8604.

534 (18)   Clark, E. L.; Hahn, C.; Jaramillo, T. F.; Bell, A. T., Electrochemical CO_2 Reduction
535 over Compressively Strained CuAg Surface Alloys with Enhanced Multi-Carbon Oxygenate
536 Selectivity. *J. Am. Chem. Soc.* **2017,** *139*, 15848-15857.
537 (19)   Higgins, D.; Landers, A. T.; Ji, Y.; Nitopi, S.; Morales-Guio, C. G.; Wang, L.; Chan,
538 K.; Hahn, C.; Jaramillo, T. F., Guiding Electrochemical Carbon Dioxide Reduction toward
539 Carbonyls Using Copper Silver Thin Films with Interphase Miscibility. *ACS Energy Lett.* **2018,**
540 *3*, 2947-2955.
541 (20)   Chang, Z.; Huo, S.; Zhang, W.; Fang, J.; Wang, H., The Tunable and Highly Selective
542 Reduction Products on Ag@Cu Bimetallic Catalysts toward CO_2 Electrochemical Reduction
543 Reaction. *J. Phys. Chem. C* **2017,** *121*, 11368-11379.
544 (21)   Li, Y. C.; Wang, Z.; Yuan, T.; Nam, D.-H.; Luo, M.; Wicks, J.; Chen, B.; Li, J.; Li, F.;
545 de Arquer, F. P. G.; Wang, Y.; Dinh, C.-T.; Voznyy, O.; Sinton, D.; Sargent, E. H., Binding
546 Site Diversity Promotes CO_2 Electroreduction to Ethanol. *J. Am. Chem. Soc.* **2019,** *141*, 8584-
547 8591.
548 (22)   Hoang, T. T. H.; Verma, S.; Ma, S.; Fister, T. T.; Timoshenko, J.; Frenkel, A. I.; Kenis,
549 P. J. A.; Gewirth, A. A., Nanoporous Copper–Silver Alloys by Additive-Controlled
550 Electrodeposition for the Selective Electroreduction of CO_2 to Ethylene and Ethanol. *J. Am.*
551 *Chem. Soc.* **2018,** *140*, 5791-5797.
552 (23)   Wang, J.; Li, Z.; Dong, C.; Feng, Y.; Yang, J.; Liu, H.; Du, X., Silver/Copper Interface
553 for Relay Electroreduction of Carbon Dioxide to Ethylene. *ACS Appl. Mater. Interfaces* **2019,**
554 *11*, 2763-2767.
555 (24)   Lum, Y.; Ager, J. W., Sequential Catalysis Controls Selectivity in Electrochemical CO_2
556 Reduction on Cu. *Energy Environ. Sci.* **2018,** *11*, 2935-2944.
557 (25)   Huang, J.; Mensi, M.; Oveisi, E.; Mantella, V.; Buonsanti, R., Structural Sensitivities
558 in Bimetallic Catalysts for Electrochemical CO_2 Reduction Revealed by Ag–Cu Nanodimers.
559 *J. Am. Chem. Soc.* **2019,** *141*, 2490-2499.
560 (26)   Gurudayal; Perone, D.; Malani, S.; Lum, Y.; Haussener, S.; Ager, J. W., Sequential
561 Cascade Electrocatalytic Conversion of Carbon Dioxide to C-C Coupled Products. *ACS Appl.*
562 *Energy Mater.* **2019,** *2*, 4551-4559.
563 (27)   Gao, J.; Zhang, H.; Guo, X.; Luo, J.; Zakeeruddin, S. M.; Ren, D.; Grätzel, M., Selective
564 C–C Coupling in Carbon Dioxide Electroreduction via Efficient Spillover of Intermediates As
565 Supported by Operando Raman Spectroscopy. *J. Am. Chem. Soc.* **2019,** *141*, 18704-18714.
566 (28)   Tan, Y.; Xue, X.; Peng, Q.; Zhao, H.; Wang, T.; Li, Y., Controllable Fabrication and
567 Electrical Performance of Single Crystalline Cu_2O Nanowires with High Aspect Ratios. *Nano*
568 *Lett.* **2007,** *7*, 3723-3728.
569 (29)   Mandal, L.; Yang, K. R.; Motapothula, M. R.; Ren, D.; Lobaccaro, P.; Patra, A.;
570 Sherburne, M.; Batista, V. S.; Yeo, B. S.; Ager, J. W.; Martin, J.; Venkatesan, T., Investigating
571 the Role of Copper Oxide in Electrochemical CO_2 Reduction in Real Time. *ACS Appl. Mater.*
572 *Interfaces* **2018,** *10*, 8574-8584.
573 (30)   Scholten, F.; Sinev, I.; Bernal, M.; Roldan Cuenya, B., Plasma-Modified Dendritic Cu
574 Catalyst for CO_2 Electroreduction. *ACS Catal.* **2019,** *9*, 5496-5502.
575 (31)   Nag, S.; Mahdak, K. C.; Devaraj, A.; Gohil, S.; Ayyub, P.; Banerjee, R., Phase
576 Separation in Immiscible Silver–Copper Alloy Thin Films. *J. Mater. Sci.* **2009,** *44*, 3393-3401.
577 (32)   Lu, Q.; Rosen, J.; Zhou, Y.; Hutchings, G. S.; Kimmel, Y. C.; Chen, J. G.; Jiao, F., A
578 Selective and Efficient Electrocatalyst for Carbon Dioxide Reduction. *Nat. Commun.* **2014,** *5*,
579 3242.
580 (33)   Hatsukade, T.; Kuhl, K. P.; Cave, E. R.; Abram, D. N.; Jaramillo, T. F., Insights into
581 the Electrocatalytic Reduction of CO_2 on Metallic Silver Surfaces. *Phys. Chem. Chem. Phys.*
582 **2014,** *16*, 13814-13819.

583 (34) Hanselman, S.; Koper, M. T. M.; Calle-Vallejo, F., Computational Comparison of Late
584 Transition Metal (100) Surfaces for the Electrocatalytic Reduction of CO to C_2 Species. *ACS*
585 *Energy Lett.* **2018,** *3*, 1062-1067.
586 (35) Zhang, H.; Chang, X.; Chen, J. G.; Goddard, W. A.; Xu, B.; Cheng, M.-J.; Lu, Q.,
587 Computational and Experimental Demonstrations of One-Pot Tandem Catalysis for
588 Electrochemical Carbon Dioxide Reduction to Methane. *Nat. Commun.* **2019,** *10*, 3340.
589 (36) Cavalca, F.; Ferragut, R.; Aghion, S.; Eilert, A.; Diaz-Morales, O.; Liu, C.; Koh, A. L.;
590 Hansen, T. W.; Pettersson, L. G. M.; Nilsson, A., Nature and Distribution of Stable Subsurface
591 Oxygen in Copper Electrodes During Electrochemical CO_2 Reduction. *J. Phys. Chem. C* **2017,**
592 *121*, 25003-25009.
593 (37) Liu, C.; Lourenço, M. P.; Hedström, S.; Cavalca, F.; Diaz-Morales, O.; Duarte, H. A.;
594 Nilsson, A.; Pettersson, L. G. M., Stability and Effects of Subsurface Oxygen in Oxide-Derived
595 Cu Catalyst for CO_2 Reduction. *J. Phys. Chem. C* **2017,** *121*, 25010-25017.
596 (38) Garza, A. J.; Bell, A. T.; Head-Gordon, M., Is Subsurface Oxygen Necessary for the
597 Electrochemical Reduction of CO_2 on Copper? *J. Phys. Chem. Lett.* **2018,** *9*, 601-606.
598 (39) Fields, M.; Hong, X.; Nørskov, J. K.; Chan, K., Role of Subsurface Oxygen on Cu
599 Surfaces for CO_2 Electrochemical Reduction. *J. Phys. Chem. C* **2018,** *122*, 16209-16215.
600 (40) Lum, Y.; Ager, J. W., Evidence for Product-Specific Active Sites on Oxide-Derived Cu
601 Catalysts for Electrochemical CO_2 Reduction. *Nat. Catal.* **2019,** *2*, 86-93.
602 (41) Okamoto, H.; Chakrabarti, D. J.; Laughlin, D. E.; Massalski, T. B., The Au-Cu (Gold-
603 Copper) System. *Bull. Alloy Phase Diagr.* **1987,** *8*, 454-473.
604 (42) Sauthoff, G., *Intermetallics.* Wiley-VCH Verlag GmbH & Co. KGaA.: Weinheim,
605 Germany, 2006; p 646-766.
606 (43) Bagger, A.; Arán-Ais, R. M.; Halldin Stenlid, J.; Campos dos Santos, E.; Arnarson, L.;
607 Degn Jensen, K.; Escudero-Escribano, M.; Roldan Cuenya, B.; Rossmeisl, J., Ab Initio Cyclic
608 Voltammetry on Cu(111), Cu(100) and Cu(110) in Acidic, Neutral and Alkaline Solutions.
609 *ChemPhysChem* **2019,** *20*, 3096-3105.
610 (44) Mistry, H.; Choi, Y.-W.; Bagger, A.; Scholten, F.; Bonifacio, C. S.; Sinev, I.; Divins,
611 N. J.; Zegkinoglou, I.; Jeon, H. S.; Kisslinger, K.; Stach, E. A.; Yang, J. C.; Rossmeisl, J.;
612 Roldan Cuenya, B., Enhanced Carbon Dioxide Electroreduction to Carbon Monoxide over
613 Defect-Rich Plasma-Activated Silver Catalysts. *Angew. Chem. Int. Ed.* **2017,** *56*, 11394-11398.
614 (45) Peterson, A. A.; Abild-Pedersen, F.; Studt, F.; Rossmeisl, J.; Norskov, J. K., How
615 Copper Catalyzes the Electroreduction of Carbon Dioxide into Hydrocarbon Fuels. *Energy*
616 *Environ. Sci.* **2010,** *3*, 1311-1315.
617 (46) Jiang, K.; Sandberg, R. B.; Akey, A. J.; Liu, X.; Bell, D. C.; Nørskov, J. K.; Chan, K.;
618 Wang, H., Metal Ion Cycling of Cu Foil for Selective C–C Coupling in Electrochemical CO_2
619 Reduction. *Nat. Catal.* **2018,** *1*, 111-119.
620 (47) Nitopi, S.; Bertheussen, E.; Scott, S. B.; Liu, X.; Engstfeld, A. K.; Horch, S.; Seger, B.;
621 Stephens, I. E. L.; Chan, K.; Hahn, C.; Nørskov, J. K.; Jaramillo, T. F.; Chorkendorff, I.,
622 Progress and Perspectives of Electrochemical CO_2 Reduction on Copper in Aqueous
623 Electrolyte. *Chem. Rev.* **2019,** *119*, 7610-7672.
624 (48) Wang, J.; Sun, Q.; Chan, S.; Su, H., The Acceleration of Methanol Synthesis and C_2
625 Oxygenates Formation on Copper Grain Boundary from Syngas. *Appl. Catal., A* **2016,** *509*,
626 97-104.
627 (49) Ma, S.; Sadakiyo, M.; Luo, R.; Heima, M.; Yamauchi, M.; Kenis, P. J. A., One-Step
628 Electrosynthesis of Ethylene and Ethanol from CO_2 in an Alkaline Electrolyzer. *J. Power*
629 *Sources* **2016,** *301*, 219-228.
630 (50) Bagger, A.; Arnarson, L.; Hansen, M. H.; Spohr, E.; Rossmeisl, J., Electrochemical CO
631 Reduction: A Property of the Electrochemical Interface. *J. Am. Chem. Soc.* **2019,** *141*, 1506-
632 1514.

633 (51)   Wang, S.; Petzold, V.; Tripkovic, V.; Kleis, J.; Howalt, J. G.; Skúlason, E.; Fernández,
634 E. M.; Hvolbæk, B.; Jones, G.; Toftelund, A.; Falsig, H.; Björketun, M.; Studt, F.; Abild-
635 Pedersen, F.; Rossmeisl, J.; Nørskov, J. K.; Bligaard, T., Universal Transition State Scaling
636 Relations for (De)hydrogenation over Transition Metals. *Phys. Chem. Chem. Phys.* **2011,** *13*,
637 20760-20765.
638 (52)   Wang, S.; Temel, B.; Shen, J.; Jones, G.; Grabow, L.; Studt, F.; Bligaard, T.; Abild-
639 Pedersen, F.; Christensen, C.; Nørskov, J., Universal Brønsted-Evans-Polanyi Relations for C-
640 C, C-O, C-N, N-O, N-N, and O-O Dissociation Reactions. *Catal. Lett.* **2011,** *141*, 370-373.
641 (53)   Clark, E. L.; Wong, J.; Garza, A. J.; Lin, Z.; Head-Gordon, M.; Bell, A. T., Explaining
642 the Incorporation of Oxygen Derived from Solvent Water into the Oxygenated Products of CO
643 Reduction over Cu. *J. Am. Chem. Soc.* **2019,** *141*, 4191-4193.
644 (54)   Lum, Y.; Cheng, T.; Goddard, W. A.; Ager, J. W., Electrochemical CO Reduction
645 Builds Solvent Water into Oxygenate Products. *J. Am. Chem. Soc.* **2018,** *140*, 9337-9340.
646 (55)   Li, H.; Li, Y.; Koper, M. T. M.; Calle-Vallejo, F., Bond-Making and Breaking between
647 Carbon, Nitrogen, and Oxygen in Electrocatalysis. *J. Am. Chem. Soc.* **2014,** *136*, 15694-15701.
648 (56)   Durand, W. J.; Peterson, A. A.; Studt, F.; Abild-Pedersen, F.; Nørskov, J. K., Structure
649 Effects on the Energetics of the Electrochemical Reduction of CO_2 by Copper Surfaces. *Surf.*
650 *Sci.* **2011,** *605*, 1354-1359.
651 (57)   Montoya, J. H.; Peterson, A. A.; Nørskov, J. K., Insights into C-C Coupling in CO_2
652 Electroreduction on Copper Electrodes. *ChemCatChem* **2013,** *5*, 737-742.
653 (58)   Kresse, G.; Furthmüller, J., Efficient Iterative Schemes for Ab Initio Total-Energy
654 Calculations Using a Plane-Wave Basis Set. *Phys. Rev. B* **1996,** *54*, 11169-11186.
655 (59)   Perdew, J. P.; Burke, K.; Ernzerhof, M., Generalized Gradient Approximation Made
656 Simple. *Phys. Rev. Lett.* **1996,** *77*, 3865-3868.
657 (60)   Kresse, G.; Joubert, D., From Ultrasoft Pseudopotentials to the Projector Augmented-
658 Wave Method. *Phys. Rev. B* **1999,** *59*, 1758-1775.
659 (61)   Monkhorst, H. J.; Pack, J. D., Special Points for Brillouin-Zone Integrations. *Phys. Rev.*
660 *B* **1976,** *13*, 5188-5192.
661 (62)   He, Z.-D.; Hanselman, S.; Chen, Y.-X.; Koper, M. T. M.; Calle-Vallejo, F., Importance
662 of Solvation for the Accurate Prediction of Oxygen Reduction Activities of Pt-Based
663 Electrocatalysts. *J. Phys. Chem. Lett.* **2017,** *8*, 2243-2246.
664 (63)   Henkelman, G.; Uberuaga, B. P.; Jónsson, H., A Climbing Image Nudged Elastic Band
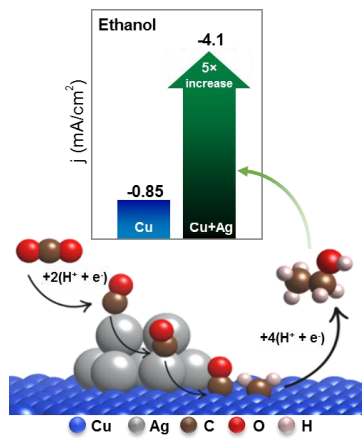665 Method for Finding Saddle Points and Minimum Energy Paths. *J. Chem. Phys.* **2000,** *113*,
666 9901-9904.

667

668

669

670   TOC Figure

671

672